HHS Public Access

Author manuscript

Adv Mater. Author manuscript; available in PMC 2020 May 01.

Published in final edited form as:

Adv Mater. 2019 May ; 31(19): e1900401. doi:10.1002/adma.201900401.

Wet/Sono-Chemical Synthesis of Enzymatic Two-Dimensional MnO_2 Nanosheets for Synergistic Catalysis-Enhanced Phototheranostics

Wei Tang,
Laboratory of Molecular Imaging and Nanomedicine (LOMIN), National Institute of Biomedical Imaging and Bioengineering (NIBIB), National Institutes of Health (NIH), Bethesda, MD 20892, USA

Wenpei Fan,
Laboratory of Molecular Imaging and Nanomedicine (LOMIN), National Institute of Biomedical Imaging and Bioengineering (NIBIB), National Institutes of Health (NIH), Bethesda, MD 20892, USA

Weizhong Zhang,
Department of Chemistry, University of Georgia, Athens, GA 30602, USA

Zhen Yang,
Laboratory of Molecular Imaging and Nanomedicine (LOMIN), National Institute of Biomedical Imaging and Bioengineering (NIBIB), National Institutes of Health (NIH), Bethesda, MD 20892, USA

Ling Li,
Laboratory of Molecular Imaging and Nanomedicine (LOMIN), National Institute of Biomedical Imaging and Bioengineering (NIBIB), National Institutes of Health (NIH), Bethesda, MD 20892, USA

Zhantong Wang,
Laboratory of Molecular Imaging and Nanomedicine (LOMIN), National Institute of Biomedical Imaging and Bioengineering (NIBIB), National Institutes of Health (NIH), Bethesda, MD 20892, USA

Ya-Ling Chiang,
Laboratory of Cellular Imaging and Macfromolecular Biophysics, National Institute of Biomedical Imaging and Bioengineering (NIBIB), National Institutes of Health (NIH), Bethesda, MD 20892, USA

Yijing Liu,
Laboratory of Molecular Imaging and Nanomedicine (LOMIN), National Institute of Biomedical Imaging and Bioengineering (NIBIB), National Institutes of Health (NIH), Bethesda, MD 20892, USA

shawn.chen@nih.gov, wenpei.fan@nih.gov, jinxie@uga.edu.

Supporting Information

Supporting Information is available from the Wiley Online Library or from the author.

Liming Deng,
Laboratory of Molecular Imaging and Nanomedicine (LOMIN), National Institute of Biomedical Imaging and Bioengineering (NIBIB), National Institutes of Health (NIH), Bethesda, MD 20892, USA

Liangcan He,
Laboratory of Molecular Imaging and Nanomedicine (LOMIN), National Institute of Biomedical Imaging and Bioengineering (NIBIB), National Institutes of Health (NIH), Bethesda, MD 20892, USA

Zheyu Shen,
Laboratory of Molecular Imaging and Nanomedicine (LOMIN), National Institute of Biomedical Imaging and Bioengineering (NIBIB), National Institutes of Health (NIH), Bethesda, MD 20892, USA

Orit Jacobson,
Laboratory of Molecular Imaging and Nanomedicine (LOMIN) National Institute of Biomedical Imaging and Bioengineering (NIBIB) National Institutes of Health (NIH) Bethesda, MD 20892, USA

Maria A. Aronova,
Laboratory of Cellular Imaging and Macfromolecular Biophysics, National Institute of Biomedical Imaging and Bioengineering (NIBIB), National Institutes of Health (NIH), Bethesda, MD 20892, USA

Albert Jin,
Laboratory of Cellular Imaging and Macfromolecular Biophysics, National Institute of Biomedical Imaging and Bioengineering (NIBIB), National Institutes of Health (NIH), Bethesda, MD 20892, USA

Jin Xie, and
Department of Chemistry, University of Georgia, Athens, GA 30602, USA

Xiaoyuan Chen
Laboratory of Molecular Imaging and Nanomedicine (LOMIN), National Institute of Biomedical Imaging and Bioengineering (NIBIB), National Institutes of Health (NIH), Bethesda, MD 20892, USA

Abstract

Two-dimensional (2D) nanomaterial has attracted broad interest in the field of biomedicine owing to their large surface area, high drug loading capacity, and excellent photothermal conversion. However, few studies report their “enzyme-like” catalytic performance because current synthetic protocols are difficult to prepare enzymatic nanosheets with small size and ultrathin thickness. Herein, a novel one-step wet-chemical method is first proposed for protein-directed synthesis of 2D MnO_2 nanosheets, in which the size and thickness can be easily adjusted by the protein dosage. Then a unique sono-chemical approach is introduced for surface-functionalization of the MnO_2 nanosheets with high dispersity/stability as well as metal cation chelating capacity, which can not only chelate ^{64}Cu radionuclides for PET imaging, but also capture the potentially released Mn^{2+} for enhanced biosafety. Interestingly, the resulting M-NS exhibits excellent enzyme-like

activity to catalyze the oxidation of glucose, which represents an alternative paradigm of acute glucose oxidase (GO*x*) for starving cancer cells and sensitizing them to thermal ablation. Featured with outstanding phototheranostic performance, the well-designed M-NS can achieve effective photoacoustic imaging-guided synergistic starvation-enhanced photothermal therapy. This study is expected to establish a new enzymatic phototheranostic paradigm based on small-sized and ultrathin MnO_2 nanosheets, which will broaden the application of 2D nanomaterials.

Graphical Abstract

A two-dimensional (2D) enzymatic MnO_2 nanosheet, M-NS, is developed by a novel one-step wet-chemical synthesis and followed by a unique sono-chemical modification. The M-NS, with a small and ultrathin morphology, exhibits intriguing glucose oxidase-like catalytic activity and excellent phototheranostics performance. An effective photoacoustic imaging-guided synergistic starvation-enhanced photothermal therapy is successfully achieved, broadening the application of 2D nanomaterials in biomedicine.

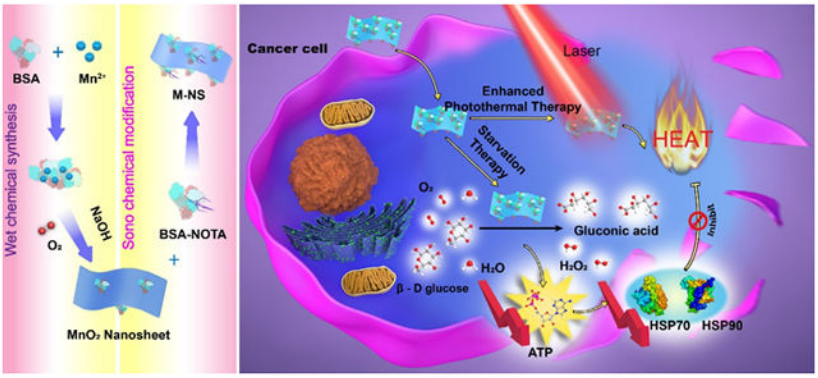

Keywords

two-dimensional nanosheets; wet-chemical synthesis; sono-chemical modification; nanozymes; phototheranostics

---

The revolutionary advances in nanosynthetic chemistry have catalyzed the naissance of two-dimensional (2D) nanomaterials with ever-growing research interest.[1, 2] The outstanding chemical, mechanical, optical, and biological properties offer unprecedented opportunities for 2D nanomaterials to be used in a wide range of fields, including optoelectronics,[3] energy conversion,[4] drug delivery,[5] tissue engineering,[6] biosensors,[7] and especially in the respect of nanomedicine.[1] For instance, the usually large surface area endows graphene oxide and black phosphorus nanosheets with a rather high drug loading capacity for enhanced chemotherapy.[8] The strong near infrared (NIR) absorbance features transition metal dichalcogenides (TMDs) and MXenes with high photothermal conversion efficiency for photothermal-mediated tumor eradication.[9] Particularly, by carefully controlling the size and thickness, 2D nanomaterials may demonstrate unexpectedly “enzyme-like” activity, which promises significant applications in catalytic therapy, an emerging cancer-therapeutic modality.[10] These so-called “artificial enzymes” exhibit unique superiorities over natural enzymes, such as easier fabrication, lower cost, and higher stability.[11] Unfortunately, there

are very few reports on the 2D nanozymes as only the small-sized and ultrathin nanosheets can exhibit superior enzymatic activity, which thus poses stringent requirements on the synthetic methods for preparation of the pointed 2D nanomaterials.

To date, a number of synthetic protocols have been established for the preparation of various families of 2D nanomaterials.[12, 13] For example, the mechanical-exfoliation approach was used to synthesize graphene nanosheets,[1] however, this method is limited by the relatively low throughput. Liquid-phase exfoliation of layered bulk crystals was suitable for large-scale production of TMD nanosheets,[14] but this method contains multiple time-consuming steps and usually yields impure products. Different from the above two top-down methods based on the exfoliation of layered bulk crystals, the chemical vapor deposition (CVD) served as a typical bottom-up method to directly produce high-quality ultrathin nanosheets with atomic thickness.[15] Nevertheless, the CVD approach yielded nanosheets are usually too large to be suitable for biomedical applications. On this ground, a facile yet effective synthetic protocol remains to be explored for generation of small-sized and ultrathin nanosheets with desirable enzymatic performance.

Herein, we propose a novel one-step wet-chemical method for protein-directed controllable synthesis of 2D MnO_2 nanosheets. The size and thickness of the MnO_2 nanosheets can be simply tuned by changing the ratio between bovine serum albumin (BSA) and Mn^{2+}. Furthermore, by surface modification with 2-S-(4-Isothiocyanatobenzyl)-1,4,7-triazacyclononane-1,4,7-triacetic acid modified BSA (BSA-NOTA) through an unreported sono-chemical synthesis avenue, the obtained BSA-NOTA-modified MnO_2 nanosheet (M-NS) exhibits extremely high dispersity/stability and versatile surface chemistry for further functionalization. For example, the NOTA in the M-NS can chelate radionuclides for PET imaging as well as capture the potentially released Mn^{2+} for reduced toxicity. Our proposed M-NS synthesis strategy is significantly different from those of other MnO_2 nanosheets or nanoparticles. For instance, MnO_2 nanosheets have been prepared by an exfoliation approach for pH- and reducing-responsive T_1-weighted magnetic resonance tumor imaging as well as photothermal therapy.[16] Spherical MnO_2 nanoparticles have been synthesized by an *in situ* redox reaction between $KMnO_4$ and reductants such as BSA, human serum albumin (HSA), and thiol groups, for glutathione (GSH) determination to detect cancer cells,[17] for O_2 generation to overcome tumor hypoxia-associated resistance to cancer therapies,[18] and for simultaneous Fenton-like reaction and GSH depletion for chemodynamic therapy of cancer.[19] Surprisingly, the well-designed small-sized and ultrathin M-NS shows fascinating glucose oxidase (GO*x*)-like activity, which can convert glucose and oxygen into gluconic acid and H_2O_2, resulting in glucose deprivation for cancer starvation therapy.[10] Moreover, the NIR-absorbing M-NS acts as an excellent paradigm of phototheranostic agents for photoacoustic (PA) imaging and photothermal therapy (PTT). Synergy with the anaerobic glycolysis metabolism disruption-mediated down-regulation of heat shock protein (HSP), the M-NS can sensitize cancer cells to heat destruction and achieve a more effective photoablation even at a mild hyperthermia temperature.[13, 20] In addition to providing a newcomer (instead of GO*x*) for enzyme-catalyzed starvation therapy by consuming intratumoral glucose, this study also explores the unprecedented “one material fits all” application of simple, powerful, and morphology-controllable 2D nanomaterials for synergistic cancer starvation-enhanced PTT under significant PA imaging guidance.

The 2D small-sized and ultrathin M-NS was synthesized *via* a distinct wet-chemical method (Figure 1a). Briefly, 6 mg of BSA was introduced to direct the nucleation of 15.1 mg of $MnCl_2$. The Mn^{2+} was spontaneously oxidized with oxygen in alkaline solutions to form MnO_2 nanosheets. Then a unique sono-chemical method was introduced to modify the MnO_2 nanosheets with BSA-NOTA (Figure 1a). The imparted BSA moiety could further stabilize the resulting BSA-NOTA modified MnO_2 nanosheet (M-NS) and improve its dispersity in PBS solution, while the NOTA moiety could chelate radioactive ^{64}Cu for PET imaging as well as capture potentially released free Mn^{2+} ions for enhanced biosafety.[21]

To achieve a uniform 2D morphology with small size and ultrathin thickness, the BSA concentration in the wet-chemical synthesis was carefully tuned from 0.6, 3, 6, 12, 30, to 60 mg (i.e., from 0.1, 0.5, 1, 2, 5, to 10-fold). After sono-chemical modification with BSA-NOTA, the resulting M-NSs were subjected to transmission electron microscope (TEM) and atomic force microscope (AFM) analysis (Figure 1b and c). While irregular shaped nanostructures (a mixture of nanorod and nanosheet) were synthesized at a low BSA concentration (0.1-fold), uniform distribution of ultrathin 2D nanosheets was achieved when increasing the BSA concentration to 1-fold. However, further elevating the BSA concentration to 5- or 10-fold transformed the nanosheets to rod-like nanostructures. The hydrodynamic diameters of the M-NSs decreased from 295.9 ± 40.6 to 105.4 ± 11.7 nm, and then increased to 343.9 ± 47.0 nm as the BSA concentration increased from 0.1- to 1- and to 10-fold (Figure S1). Correspondingly, the thickness decreased from 17.2 nm to 1.5 nm and then increased to 10.9 nm (Figure 1c **and** S2). All these observations suggested that the morphology of the M-NS could be modulated by adjusting the concentration of BSA. The optimized formulation turned out to be an initial weight ratio of 2.5 between $MnCl_2$ and BSA, in which case an ultrathin M-NS with an average diameter of 105.4 ± 11.7 nm (PDI value = 0.26) and an average thickness of around 1.5 nm was produced (Figure 1 **and** S3). The optimized M-NS exhibited excellent collodial stability in various media (Figure S4) with negilible Mn^{2+} release (Figure S5). The nanosheet structure well retained in mildly acidic (pH 6.5) and H_2O_2-overproducing (100 μM) tumor microenvrionment (TME)-mimic conditions[22] for at least 24 hours (Figure S6). This BSA-dose dependent morphology change of MnO_2 nanostructures is likely attributed to the abundance of the BSA-directed nucleation sites.[23] Distinct from other reported BSA-templated nanomaterials, which usually exhibit nanoparticle,[18, 24] nanocluster,[25] or microsphere[26] structures, an unusual ultrathin 2D nanosheet morphology was first successfully prepared *via* this novel “wet-chemical synthesis” method, revealing new insights on morphology control in the protein-directed biomineralization strategy.

The elemental mapping analysis on the optimized M-NS (1 X) exhibited homogeneous distribution of Mn and O throughout the whole nanosheet (Figure 2a). The energy-dispersive X-ray spectroscopy (EDS) data confirmed the Mn and O as the main components (Figure 2b). The powder X-ray diffraction (XRD) analysis showed an amorphous state (Figure 2c), which was further verified by the selected area electron diffraction (SAED) pattern (Figure 2d). In addition, the X-ray photoelectron spectroscopy (XPS) data confirmed the +4 valence state of Mn by exhibiting the Mn $2p_{1/2}$ and $2p_{3/2}$ peaks at around 641.5 eV and 653.2 eV,

respectively (Figure 2e and f). Taken together, the 2D M-NS structure was successfully constructed through this facile BSA-templated wet-chemical synthesis approach.

The optical properties of the M-NSs were carefully investigated. The UV-Vis-NIR spectra of M-NS (1 X) at different concentrations showed a relatively high absorption in the NIR range (Figure 2g). The absorbance intensity at 808 nm over the well length (A/L) displayed a positively linear correlation with the Mn concentration, showing an extinction coefficient of 2.68 L g^{-1} cm^{-1} according to the Lambert-Beer Law (Figure S7). In addition, the absorption spectra of all the other MnO_2 nanostructures in Figure 1 were investigated, among which the optimized M-NS formulation (1 X) exhibited the most effective NIR absorption (Figure S8). This inspired us to investigate the photoacoustic (PA) contrast and photothermal conversion of the M-NS (1 X). A positive correlation was found between the PA signal intensity and the concentration of the solutions (Figure 2h). Upon a laser irradiation (808 nm, 1 W/cm^2), the temperature of the M-NS (1 X) solution (200 μg Mn/mL) rapidly increased by 23.9 °C within 5 minutes, which was the highest value among all the BSA-templated MnO_2 nanostructures (Figure 1) at the same Mn concentration (Figure 2i **and** S9). In addition, the M-NS (1 X) demonstrated a concentration-dependent photothermal effect (Figure 2j **and** S10) and excellent stability in photothermal conversion (Figure 2k). The temperature increase wasn't compromised after four heating/cooling cycles (Figure 2k). To study the photothermal conversion efficiency, the M-NS (1 X) solution at a concentration of 200 μg Mn/mL was continuously irradiated (808 nm, 1 W/cm^2) until its temperature reached a plateau, which was measured to be an increase of 25.5 °C. The laser was then turned off to cool down the solution to room temperature (Figure 2l). According to the plot of cooling stage versus negative natural logarithm of driving force temperature (Figure S11), the photothermal efficiency of M-NS (1 X) was calculated to be 21.0 %, which is comparable to other inorganic photothermal agents, such as Cu_9S_5 nanocrystals (25.7 %),[27] $Cu_{2-x}Se$ (22 %),[28] and Au nanorods (22.1 %)[29].

Interestingly, the as-synthesized M-NSs could successfully catalyze the oxidation of glucose into gluconic acid, displaying an intriguing GO*x*-like activity (Figure 3a). The GO*x*-like activity was dependent on the MnO_2 morphologies, or the concentration of the templated BSA (Figure 3b). While an increased BSA amount enhanced the enzyme activities of the M-NS, an overdosage of BSA caused an obvious reduction in the activities. A moderate BSA dosage (1 X), with small-sized and ultrathin M-NS morphology, demonstrated the highest enzyme activity, which was a 1.68, 1.37, 1.18, 1.79, and 2.41-fold higher than that of other formulations (0.1, 0.5, 2, 5, and 10-fold BSA dosages, respectively, Figure 3c). This morphology-dependent GO*x*-like activity of the 2D MnO_2 nanozyme is ascribed to the size effects.[23] A smaller size and thinner thickness led to a larger surface area, implying more active sites and better dispersity of the M-NS for enhanced enzymatic activity. Therefore, the small-sized and ultrathin M-NS synthesized based on the 1 X of BSA dosage would be used in the subsequent *in vitro* and *in vivo* studies.

Next, the catalytic performance of the M-NS was carefully investigated based on the typical Michaelis-Menten steady-state enzyme kinetic assay.[30] A series of glucose solutions were applied as the substrates. The Michaelis–Menten constant (K_M) and maximum velocity (V_{max}) were calculated to be 26.40 mM and 7.04×10^{-8} M s^{-1}, respectively, according to

the Michaelis–Menten curves (Figure 3d) and Lineweaver–Burk plot (Figure 3e). The K_M value of M-NS was lower than that of GO*x* (34 mM),[31] suggesting a stronger glucose affinity of M-NS nanozyme than the natural enzyme. Moreover, it is well known that the nanozyme shows a much better stability than the natural enzyme, especially in response to heat ablation.[12, 32] To test the thermostability, the catalytic activities of M-NS and GO*x* were compared after 1 h of incubation at temperatures ranging from 4 to 90 °C. The activity of GO*x* was dramatically decreased when incubated at temperature above 37 °C. Only 30 % and 19 % of the initial activity was retained at 60 and 70 °C, respectively. In sharp contrast, the M-NS retained more than 70 % of the initial activity after incubation at 4 – 80 °C for 1 h (Figure 3f). These results unambiguously demonstrated a higher thermal stability of the M-NS than that of natural GO*x*. The M-NS also retained GO*x*-like activity in acidic and H_2O_2-overproducing TME, showing over 80% of the inital activity after incubation in H_2O_2 solution (100 μM) at pH 6.5 overnight (Figure S12). In addition to GO*x*-like catalytic activity, the M-NS showed intritic peroxidase (POD)-like catalytic activity but could not effectively induce hydroxyl radical (·OH) generation in H_2O_2 aqueous solution (Figure S13). The M-NS exhibited redox reaction capacity rather than catalytic performance to GSH and ascorbic acid (Figure S14).

GO*x* has been widely studied for starvation therapy.[10, 13, 33] By disrupting the glucose metabolism in cells, the GO*x* can inhibit anaerobic glycolysis, thereby suppressing ATP production,[34] which is essential for cell growth and protein synthesis. These include heat shock proteins (HSPs), a family of proteins that are known to be involved in thermoresistance of cells.[13, 35] The inhibited HSP expression, in turn, will increase the sensitivity of cancer cells to thermal ablation.[13, 20, 36] Given the excellent GO*x*-like activity (Figure 3d - f) and photothermal capacity (Figure 2j -l), it was reasonably hypothesized that the M-NS, upon cellular uptake, could induce glucose deprivation and HSP down-regulation, leading to combinational starvation and PTT (Figure 4a). To investigate M-NS-mediated glycolysis inhibition, U87MG cells were incubated with M-NS and the cellular ATP concentration was measured over the incubation time. As shown in Figure 4b, the ATP level dropped to 71.9, 57.8, 29.3, and 13.5 % after co-incubation with the M-NS for 1, 4, 12, and 24 hours, respectively. In addition, reduced cellular gluocse level was observed correspondingly (Figure S15). This dysfunctional glycolytic pathway could ultimately interfere with cellular HSP level.[13, 20] The Western blot analysis on two main HSP members, HSP90 and HSP70, in U87MG cells exhibited a significant reduced expression after co-incubation with M-NS (Figure 4c). For positive controls, cells were incubated overnight at a mild hyperthermia temperature of 40 °C, in which case a significantly elevated expression of HSP90 and HSP70 was observed.[35] Confocal microscopy analysis found the same change of HSP expression (Figure 4d). Furthermore, increased intracellular reactive oxygen speices (ROS) production was found in U87MG cells over the co-incubation with M-NS (Figure S16), which may be ascribed to increased H_2O_2 generation by the M-NS-catalyzed glucose oxidization as well as the intracellular GSH consumption (Figure S17).[19]

After consolidating the *in vitro* GO*x*-like enzyme activity, the synergy between the starvation therapy and low-temperature PTT [13] was investigated by MTT assay. Interestingly, even at a concentration as low as 12 μg Mn/mL, M-NS treatment still

decreased the cell viability by ~30 % (Figure S18). As a comparison, other MnO_2 nanoparticles were reported to be non-toxic at this concentration[16] (Figure S19). Further increasing the M-NS concentration to 50 μg Mn/mL didn't affect much on the cell toxicity. This little correlation between the M-NS concentration and its induced cell cytotoxicity well suggested the enzyme-catalytic activity of the M-NS for cancer cell starvation. In typical enzyme-catalyzed reactions, a very low concentration of enzyme is usually enough for the catalysis, and the reaction products are only dependent on the concentration of substrate but not the enzyme.[30] The M-NS had much lower catalytic efficiency to nomrmal cells (Figure S20). Next, to investigate the synergistic effect, the cells were incubated with M-NS and followed by a five minutes of laser irradiation (808 nm, 1 W/cm^2). In controls, the cells were treated with M-NS, laser irradiation, or PBS. The combination treatment group (M-NS + NIR) significantly decreased the cell viability to 30.2 %, which was much lower than that of the starvation therapy only group (M-NS-treated, 61.1%). No obvious cell killing was observed after the exposure to the NIR irradiation, suggesting minimal side effects (Figure 4e). Live and dead assay (Figure S21) and flow cytometry analysis (Figure 4f) verified the results. The enhanced therapeutic efficacy in the combination group should be attributed to the M-NS-mediated glucose deprivation. The intracellular glucose depletion starved the cancer cells. Meanwhile, the disruption of glycolytic metabolism caused reduced ATP production, HSP expression, and cell heat-endurability, thereby sensitizing cells to M-NS-induced photothermal ablation. All these observations suggested that the M-NS was a promising theranostic agents for cancer management.

To investigate tumor accumulation, the M-NS was chelated with ^{64}Cu radionuclides *via* its surface-bound NOTA. The resulting ^{64}Cu-labeled M-NS was systematically administrated into U87MG tumor-bearing mice. The M-NS distribution was then monitored by positron emission tomography (PET) (Figure 5a). The M-NS was gradually accumulated at tumors and reached a peak of 5.92 ± 0.44 %ID/g at 24 h post-injection (p.i., Figure 5b). At 48 h p.i., the tumors and major organs were harvested and the radioactivities were measured by gamma countering (Figure S22). A relatively high signal was detected in liver (12.48 %ID/g) than that in the kidneys (5.14 %ID/g), suggesting the M-NS was mainly excreted through the reticuloendothelial system, which is typical for sub-100 nm sized inorganic nanoparticles.[37] Furthermore, the tumor uptake of M-NS was verified by PA imaging, which showed an obvious contrast enhancement in tumor areas with the highest contrast seen at 24 h p.i. (Figure 5c). The M-NS also demonstrated excellent photothermal effects (Figure 5d). When irradiated (1.0 W/cm^2) at 24 p.i., the tumor heated to 45.1 ± 1.8 °C within 3 min and maintained at 46.5 ± 1.7 °C after 5 min (Figure 5e). In sharp contrast, 1.0 W/cm^2 irradiation alone caused no significant temperature increase. In addition, the blood glucose level was carefully monitored for 24 h after intravenous administration of M-NS in balb/c mice (n = 3). In all the tested mice, the blood glucose level exhibited a transient and moderate decrease within 30 min of injection, which was recovered by 1 h p.i. (Figure S23). No pathoglycemia was observed in follow-up studies, suggesting the high bio-safety of the M-NS.

The *in vivo* biosafety of M-NS was further evaluated in normal balb/c mice *via* intravenous injection of the M-NS. The mice body weight increased steadily during the 30-day evaluation (Figure S24). Blood tests were performed at 7 and 30 days p.i. (Figure S25). The

liver functions remained normal after M-NS treatment as alanine aminotransferase (ALT), aspartate transaminase (AST), and alkaline phosphatase (AKP) levels all showed little variation compared with the PBS control groups. The blood urea nitrogen (BUN), creatinine (CREA), total protein (TP), and albumin (ALB) showed no abnormalities in the two M-NS-treated groups. Moreover, no obvious changes were found in complete blood count parameters, including white blood cells (WBC), red blood cells (RBC), platelets (PLT), mean corpuscular volume (MCV), hematocrit (HCT), and hemoglobin (HGB). In addition, histological analysis on major organ tissues was performed at the end of the evaluation. No obvious pathological abnormalities were detected in heat, lung, liver, spleen, and kidneys, indicating high histocompatibility of the M-NS (Figure S26).

Therapy studies with the M-NS were then conducted on U87MG tumor-bearing mice (Figure 5f). The mice were systematically injected with the M-NS and followed by a 5-min laser irradiation (808 nm, 1 W/cm^2) to tumors. For controls, the mice were treated with M-NS only, NIR only, or PBS. M-NS plus NIR completely eradicated tumors without recurrence. Compared with the PBS control group, the starvation therapy with M-NS caused a 62.6 ± 11.9 % tumor growth inhibition on Day 18. Meanwhile, irradiation alone had no tumor suppression effect (Figure S27). To further explore the underlying mechanisms, in a separate study, mice were sacrificed 24 hours after the treatments. Tumors were collected for H&E staining (Figure 5g) and TUNEL assays (Figure 5h and S28). In good correspondences with the tumor growth curves, severe tumor structure damage was observed in both the M-NS+NIR group and M-NS groups, but not the NIR only group. Between the M-NS+NIR and M-NS groups, the M-NS+NIR treated tumors showed a much sparser cancer cell distribution and more extensive of cell apoptosis, indicating a better treatment efficacy. It was worth noting that the PTT with M-NS was controlled to only elevate the tumor temperature to around 46.5 °C, which usually does not induce effective photoablation by itself.[38] It is postulated that the excellent tumor growth control seen with M-NS+NIR was again a result of starvation therapy induced cancer cell sensitization to thermal ablation. To investigate, the tumor sections were stained with anti-HSP70 and anti-HSP90 antibodies (Figure 5i and S29).[13, 20] With or without NIR irradiation, M-NS treatment caused remarkable reduction of HSP70 and HSP90 expression, confirming the hypothesis. The intratumoral GSH level dropped at 24 h after systemic administration of M-NS, which might also contribute to the treatment efficacy (Figure S30). Aside from tumor damage, there was no significant mice body weight drop (Figure S31) as well as no obvious pathological changes in heart, liver, lung, kidneys, and spleen (Figure S32).

In summary, we have synthesized small-sized and ultrathin MnO_2 nanosheets (M-NSs) through a novel BSA-templated “wet-chemical” synthesis method followed by functionalization/stabilization with a unique “sono-chemical” approach. By simply tuning the BSA concentration, the morphology (i.e., size and thickness) of the M-NS can be easily controlled. The smaller and thinner M-NS, the better GO*x*-like catalytic activity and photothermal conversion. The enzymatic activity-catalyzed depletion of intratumor glucose featured the M-NS an alternative paradigm of GO*x* for effective starvation therapy, which sensitizes cancer cells to thermal ablation. As a result, M-NS-mediated PTT efficiently eradicates tumors even at a relatively low temperature. The PA imaging performance and synergy between starvation therapy and PTT were demonstrated both *in vitro* and *in vivo*.

Our studies illustrate significant guidance on the design of intriguing enzymatic phototheranositcs 2D nanomaterials for cancer management.

Experimental Section

Preparation of BSA-NOTA.

NOTA-p-SCN and BSA at a molar ratio of 5:1 were mixed in 0.1 M borate buffer (pH 9.4) containing 5–10% (V/V) of DMSO overnight at 4 °C. Afterwards, the BSA-NOTA product was purified on PD10 column (GE Healthcare) using 0.1 M NaH_2PO_4 (pH 7.5) solution as an eluent. The fraction containing BSA-NOTA was concentrated by 30K Centricon (GE Healthcare) to a final concentration of 40 mg/mL as determined by Nano-drop (Fisher Scientific).

Synthesis of M-NS.

First, 15.1 mg $MnCl_2$ and a certain amount of BSA (0.6, 3, 6, 12, 30, and 60 mg) were mixed in 60 mL of ultrapure water and stirred for 1 h at room temperature. Then NaOH solution was added to the mixed solution to adjust the pH value to about 10. After stirring overnight, MnO_2 nanosheet was centrifugated and washed for three times. Second, MnO_2 nanosheet was added to 1 mL of 10 mg/mL BSA-NOTA. The mixed solution was sonicated for 20 min. The yielded M-NS (BSA-NOTA surface-modified MnO_2 nanosheet) products were centrifugated and washed for three times.

In Vitro Photothermal Performance.

An 808-nm laser irradiation at 1.0 W/cm^2 was applied in all cases. To investigate the impact of MnO_2 morphology on photothermal conversion, 200 μg/mL M-NS solutions with different BSA formulations were irradiated for 5 minutes. To examine the concentration-dependent photothermal effect, M-NS solutions at various concentrations (0, 25, 50, 100, and 200 μg/mL) were irradiated for 5 minutes. To study the photothermal stability, 200 μg/mL M-NS solution was irradiated for five repeated intervals of five min of irradiation on and five min off. To investigate the photothermal conversion efficiency, 200 μg/mL M-NS solution was irradiated for 15 min and then cooled down for another 15 min. A SC300 infrared camera was applied to monitor the solution temperature changes during the irradiation.

Glucose Oxidase-Like Activity.

To explore the impact of MnO_2 morphology on the enzyme activities, 20 ug Mn/mL solutions of M-NS templated with different BSA dosages were tested with the Glucose Oxidase Activity Assay Kit (abcam, ab219924). The absorbance at 570 nm was plotted over time after subtracting the interference from MnO_2. To investigate the influence of temperature on the GO*x*-like activity, M-NS (20 μg/mL) or GO*x* (60 mM) was incubated at different temperatures (4, 25, 37, 50, 60, 70 ,80, and 90 °C) for 1 h, respectively. Soon after that, the solutions were cooled on ice and the remaining enzyme activities were measured by the same method. To measure the enzyme kinetics, M-NS (20 μg Mn/mL) was incubated with different concentrations of glucose substrate and followed by detection with TMB system (λ = 650 nm, $\varepsilon_{650\ nm}$ = 39000 M^{-1} cm^{-1}). A set of initial velocity (v_0) values at

various concentrations of glucose ([Glucose]) was calculated by converting the initial velocity of TMB^{*+} absorbance changes *via* the Beer-Lambert law. To determine Michaelis–Menten constant (K_M) and maximal velocity (V_{max}), the Michaelis–Menten kinetic curve of M-NS ($v_0 = V_{max} * [Glucose] / ([Glucose] + K_M)$) was generated by plotting respective v_0 values against D-glucose concentrations. The Michaelis–Menten constant (K_M) and maximal velocity (V_{max}) were calculated *via* the linear double-reciprocal Lineweaver–Burk plotting ($1/v_0 = 1/V_{max} + K_M / (V_{max} * [Gluose])$).

Cellular ATP Concentration Detection.

The M-NS was co-incubated with U87MG cells at 37 °C for different durations (1, 4, 12, and 24 h). For controls, cells were incubated with PBS at 37 °C or 40 °C for 24 h in separate groups. The cells were then collected. The cellular ATP concentration was measured based on the protocol provided by the vendor (Cayman Chemical, #700410).

Cellular HSP Expression.

The M-NS was co-incubated with U87MG cells for different durations (12 and 24 hours) at 37 °C. For controls, cells were incubated with PBS for 24 h at 37 or 40 °C in separate groups. For Western blotting, cells were lysed with RIPA buffer with protease inhibitor for 10 min on ice. After centrifugation at 4 °C, the extracted proteins were separated with SDS-PAGE and then transferred to a PVDF membrane. After blocking in 5 % slim milk in TBST at room temperature for 1 h, the membrane was washed with PBST for three times. The membrane was immunoblotted with anti-HSP70 antibody, anti-HSP90 antibody, and anti-β-actin antibody overnight at 4 °C. After another wash cycle, the membrane was incubated with HRP-conjugated Goat anti-Rabbit IgG (H+L) secondary antibody for 45 min and was visualized with Western-Ready™ ECL Substrate Kit (Biolegend, 426303) according to the vendor's protocol. For immunofluorescence imaging, the cells were fixed with 4% paraformaldehyde for 10 min, permeabilized with 0.1% Triton X-100 for 5 min, and then blocked with 1% BSA in 0.1% PBST for 1 h. After washing, the slides were co-incubated with Alexa Fluor 488 conjugated Anti-HSP 70 antibody (abcam, ab204690) and Alexa Fluor 647 conjugated Anti-HSP 90 antibody (abcam, ab202823) overnight at 4 °C in a humidified atmosphere in the dark. Finally, the slides were mounted with mounting medium with DAPI and ready for confocal imaging.

Blood Glucose Measurement.

The evaluation was performed by intravenously injecting M-NS (20 mg Mn/kg) into Balb/c mice. (n = 3). Blood was drawn at selected time points (pre-injection, 0.5, 1, 2, 3, 4, 6, 8, and 24 h). Blood glucose concentration was measured with an AimStrip® Plus blood glucose meter.

Therapy Studies.

The M-NS was systematically injected into U87MG tumor-bearing mice (20 mg Mn/kg, n = 5). After 24 hours, tumors were subjected to a 1.0 W/cm^2 of 808-nm laser irradiation for 5 min. Three control groups were studied (n = 5 / group): (1) M-NS at the same injection dose (2) PBS + irradiation; and (3) PBS. Tumor growth (size = length × $width^2/2$) as well as mice

body weights were monitored every three days. In addition, tumors and major organs were collected for histological analysis.

HSP Staining.

20 μm of tumor slides were fixed with 4% paraformaldehyde for 10 min, permeabilized with 0.1% Triton X-100 for 5 min, and then blocked with 1% BSA in 0.1% PBST for 1 h. After washing, the slides were co-incubated with Alexa Fluor 488 conjugated Anti-HSP 70 antibody (abcam, ab204690) and Alexa Fluor 647 conjugated Anti-HSP 90 antibody (abcam, ab202823) overnight at 4 °C in a humidified atmosphere in the dark. The slides were then mounted with mounting medium with DAPI.

Supplementary Material

Refer to Web version on PubMed Central for supplementary material.

Acknowledgements

This work was supported by the Intramural Research Program of the National Institute of Biomedical Imaging and Bioengineering, National Institutes of Health. We thank the National Institutes of Health (R01EB022596, J.X., and R01NS093314, J.X.), and the National Science Foundation (NSF1552617, J.X.) for their funding support. We also thank the support from National Natural Science Foundation of China (51602203, W.F.) and the Youth Innovation Promotion Association of Chinese Academy of Sciences (2016269, Z.S.).

References

[1]. Chen Y, Tan C, Zhang H, Wang L, Chem. Soc. Rev. 2015, 44, 2681. [PubMed: 25519856]

[2] a). Chimene D, Alge DL, Gaharwar AK, Adv. Mater. 2015, 27, 7261; [PubMed: 26459239] b)Chen Y, Fan Z, Zhang Z, Niu W, Li C, Yang N, Chen B, Zhang H, Chem. Rev. 2018, 118, 6409. [PubMed: 29927583]

[3]. Xia F, Wang H, Xiao D, Dubey M, Ramasubramaniam A, Nat. Photon. 2014, 8, 899.

[4]. Anasori B, Lukatskaya MR, Gogotsi Y, Nat. Rev. Mater. 2017, 2, 16098.

[5] a). Shen H, Zhang LM, Liu M, Zhang ZJ, Theranostics 2012, 2, 283; [PubMed: 22448195] b)Weng Q, Wang B, Wang X, Hanagata N, Li X, Liu D, Wang X, Jiang X, Bando Y, Golberg D, ACS Nano 2014, 8, 6123. [PubMed: 24797563]

[6] a). Shin SR, Li YC, Jang HL, Khoshakhlagh P, Akbari M, Nasajpour A, Zhang YS, Tamayol A, Khademhosseini A, Adv. Drug Deliv. Rev. 2016, 105, 255; [PubMed: 27037064] b)Shin SR, Jung SM, Zalabany M, Kim K, Zorlutuna P, Kim SB, Nikkhah M, Khabiry M, Azize M, Kong J, Wan KT, Palacios T, Dokmeci MR, Bae H, Tang XW, Khademhosseini A, ACS Nano 2013, 7, 2369. [PubMed: 23363247]

[7] a). Pan YT, Yin X, Kwok KS, Yang H, Nano Lett. 2014, 14, 5953; [PubMed: 25198201] b)Gao CB, Lu ZD, Liu Y, Zhang Q, Chi MF, Cheng Q, Yin YD, Angew. Chem. Int. Ed. Engl. 2012, 51, 5629; [PubMed: 22532434] c)Li Q, Wang X, Liu Y, Wei H, Anal. Chem, 2018, 90, 9983. [PubMed: 30044077]

[8] a). Chen W, Ouyang J, Liu H, Chen M, Zeng K, Sheng J, Liu Z, Han Y, Wang L, Li J, Deng L, Liu Y-N, Guo S, Adv. Mater. 2017, 29, 1603864;b)Choi JR, Yong KW, Choi JY, Nilghaz A, Lin Y, Xu J, Lu X, Theranostics 2018, 8, 1005. [PubMed: 29463996]

[9] a). Lin H, Gao S, Dai C, Chen Y, Shi J, J. Am. Chem. Soc. 2017, 139, 16235; [PubMed: 29063760] b)Ma N, Zhang MK, Wang XS, Zhang L, Feng J, Zhang XZ, Adv. Funct. Mater. 2018, 28, 1801139.

[10]. Fu LH, Qi C, Lin J, Huang P, Chem. Soc. Rev. 2018, 47, 6454. [PubMed: 30024579]

[11] a). Fan K, Cao C, Pan Y, Lu D, Yang D, Feng J, Song L, Liang M, Yan X, Nat. Nanotechnol. 2012, 7, 459; [PubMed: 22706697] b)Zhang Y, Wang F, Liu C, Wang Z, Kang L, Huang Y, Dong

K, Ren J, Qu X, ACS Nano 2018, 12, 651; [PubMed: 29290107] c)Wang Y, Zhao M, Ping J, Chen B, Cao X, Huang Y, Tan C, Ma Q, Wu S, Yu Y, Lu Q, Chen J, Zhao W, Ying Y, Zhang H, Adv. Mater. 2016, 28, 4149; [PubMed: 27008574] d)Wu J, Wang X, Wang Q, Lou Z, Li S, Zhu Y, Qin L, Wei H, Chem. Soc. Rev. 2019, 48, 1004; [PubMed: 30534770] e)Gao L, Fan K, Yan X, Theranostics 2017, 7, 3207; [PubMed: 28900505] e)Shi S, Wu S, Shen Y, Zhang S, Xiao Y, He X, Gong J, Farnell Y, Tang Y, Huang Y, Gao L, Theranostics 2018, 8, 6149. [PubMed: 30613289]

[12]. Gao L, Zhuang J, Nie L, Zhang J, Zhang Y, Gu N, Wang T, Feng J, Yang D, Perrett S, Yan X, Nat. Nanotechnol. 2007, 2, 577. [PubMed: 18654371]

[13]. Zhou J, Li M, Hou Y, Luo Z, Chen Q, Cao H, Huo R, Xue C, Sutrisno L, Hao L, Cao Y, Ran H, Lu L, Li K, Cai K, ACS Nano 2018, 12, 2858. [PubMed: 29510031]

[14] a). Yong Y, Zhou L, Gu Z, Yan L, Tian G, Zheng X, Liu X, Zhang X, Shi J, Cong W, Yin W, Zhao Y, Nanoscale 2014, 6, 10394; [PubMed: 25047651] b)Zeng Z, Sun T, Zhu J, Huang X, Yin Z, Lu G, Fan Z, Yan Q, Hng HH, Zhang H, Angew. Chem. Int. Ed. Engl. 2012, 51, 9052. [PubMed: 22887481]

[15]. Zhan Y, Liu Z, Najmaei S, Ajayan PM, Lou J, Small 2012, 8, 966. [PubMed: 22334392]

[16]. Liu Z, Zhang S, Lin H, Zhao M, Yao H, Zhang L, Peng W, Chen Y, Biomaterials 2018, 155, 54. [PubMed: 29169038]

[17]. Wang Q, Zhang Y, Wang X, Wu Y, Dong C, Shuang S, Analyst 2019, doi: 10.1039/c8an02501k.

[18]. Lin T, Zhao X, Zhao S, Yu H, Cao W, Chen W, Wei H, Guo H, Theranostics 2018, 8, 990. [PubMed: 29463995]

[19]. Lin L, Song J, Song L, Ke K, Liu Y, Zhou Z, Shen Z, Li J, Yang Z, Tang W, Niu G, Yang H-H, Chen X, Angew. Chem. Int. Ed. Engl. 2018, 57, 4902. [PubMed: 29488312]

[20]. Chen WH, Luo GF, Lei Q, Hong S, Qiu WX, Liu LH, Cheng SX, Zhang XZ, ACS Nano 2017, 11, 1419. [PubMed: 28107631]

[21]. Xing H, Zhang S, Bu W, Zheng X, Wang L, Xiao Q, Ni D, Zhang J, Zhou L, Peng W, Zhao K, Hua Y, Shi J, Adv. Mater. 2014, 26, 3867. [PubMed: 24677351]

[22]. Zhang C, Bu W, Ni D, Zhang S, Li Q, Yao Z, Zhang J, Yao H, Wang Z, Shi J, Angew. Chem. Int. Ed. Engl. 2016, 55, 2101. [PubMed: 26836344]

[23]. Han L, Zhang HJ, Chen DY, Li F, Adv. Funct. Mater. 2018, 28, 1800018.

[24] a). Liu X, Wang Q, Zhao H, Zhang L, Su Y, Lv Y, Analyst 2012, 137, 4552; [PubMed: 22900262] b)Behrens S, Heyman A, Maul R, Essig S, Steigerwald S, Quintilla A, Wenzel W, Bürck J, Dgany O, Shoseyov O, Adv. Mater. 2009, 21, 3515.

[25]. Xie J, Zheng Y, Ying JY, J. Am. Chem. Soc. 2009, 131, 888. [PubMed: 19123810]

[26] a). Huang P, Yang D-P, Zhang C, Lin J, He M, Bao L, Cui D, Nanoscale 2011, 3, 3623; [PubMed: 21842073] b)Wang X, Yang D-P, Huang P, Li M, Li C, Chen D, Cui D, Nanoscale 2012, 4, 7766. [PubMed: 23138655]

[27]. Tian Q, Jiang F, Zou R, Liu Q, Chen Z, Zhu M, Yang S, Wang J, Wang J, Hu J, ACS Nano 2011, 5, 9761. [PubMed: 22059851]

[28]. Hessel CM, Pattani VP, Rasch M, Panthani MG, Koo B, Tunnell JW, Korgel BA, Nano Lett. 2011, 11, 2560. [PubMed: 21553924]

[29]. Zeng J, Goldfeld D, Xia Y, Angew. Chem. Int. Ed. Engl. 2013, 52, 4169. [PubMed: 23494970]

[30]. Huo M, Wang L, Chen Y, Shi J, Nat. Commun. 2017, 8, 357. [PubMed: 28842577]

[31]. Ciucu A, Pâtroescu C, Anal. Lett. 1984, 17, 1417.

[32]. Wei H, Wang E, Chem. Soc. Rev. 2013, 42, 6060. [PubMed: 23740388]

[33]. Li SY, Cheng H, Xie BR, Qiu WX, Zeng JY, Li CX, Wan SS, Zhang L, Liu WL, Zhang XZ, ACS Nano 2017, 11, 7006. [PubMed: 28665106]

[34]. Warburg O, Science 1956, 123, 309. [PubMed: 13298683]

[35] a). Ungelenk S, Moayed F, Ho CT, Grousl T, Scharf A, Mashaghi A, Tans S, Mayer MP, Mogk A, Bukau B, Nat. Commun. 2016, 7, 13673; [PubMed: 27901028] b)Calderwood SK, Gong J, Trends Biochem. Sci. 2016, 41, 311. [PubMed: 26874923]

[36] a). Wang S, Tian Y, Tian W, Sun J, Zhao S, Liu Y, Wang C, Tang Y, Ma X, Teng Z, Lu G, ACS Nano 2016, 10, 8578; [PubMed: 27576159] b)Kumar S, Stokes J 3rd, Singh UP, Gunn K.

Scissum, Acharya A, Manne U, Mishra M, Cancer Lett. 2016, 374, 156; [PubMed: 26898980] c)Chu KF, Dupuy DE, Nat. Rev. Cancer 2014, 14, 199. [PubMed: 24561446]

[37] a). Yu M, Zheng J, ACS Nano 2015, 9, 6655; [PubMed: 26149184] b)Longmire M, Choyke PL, Kobayashi H, Nanomedicine 2008, 3, 703. [PubMed: 18817471]

[38] a). Tang W, Yang Z, Wang S, Wang Z, Song J, Yu G, Fan W, Dai Y, Wang J, Shan L, Niu G, Fan Q, Chen X, ACS Nano 2018, 12, 2610; [PubMed: 29451774] b)Tang W, Fan W, Wang Z, Zhang W, Zhou S, Liu Y, Yang Z, Shao E, Zhang G, Jacobson O, Shan L, Tian R, Cheng S, Lin L, Dai Y, Shen Z, Niu G, Xie J, Chen X, ACS Nano 2018, 12, 12269. [PubMed: 30418749]

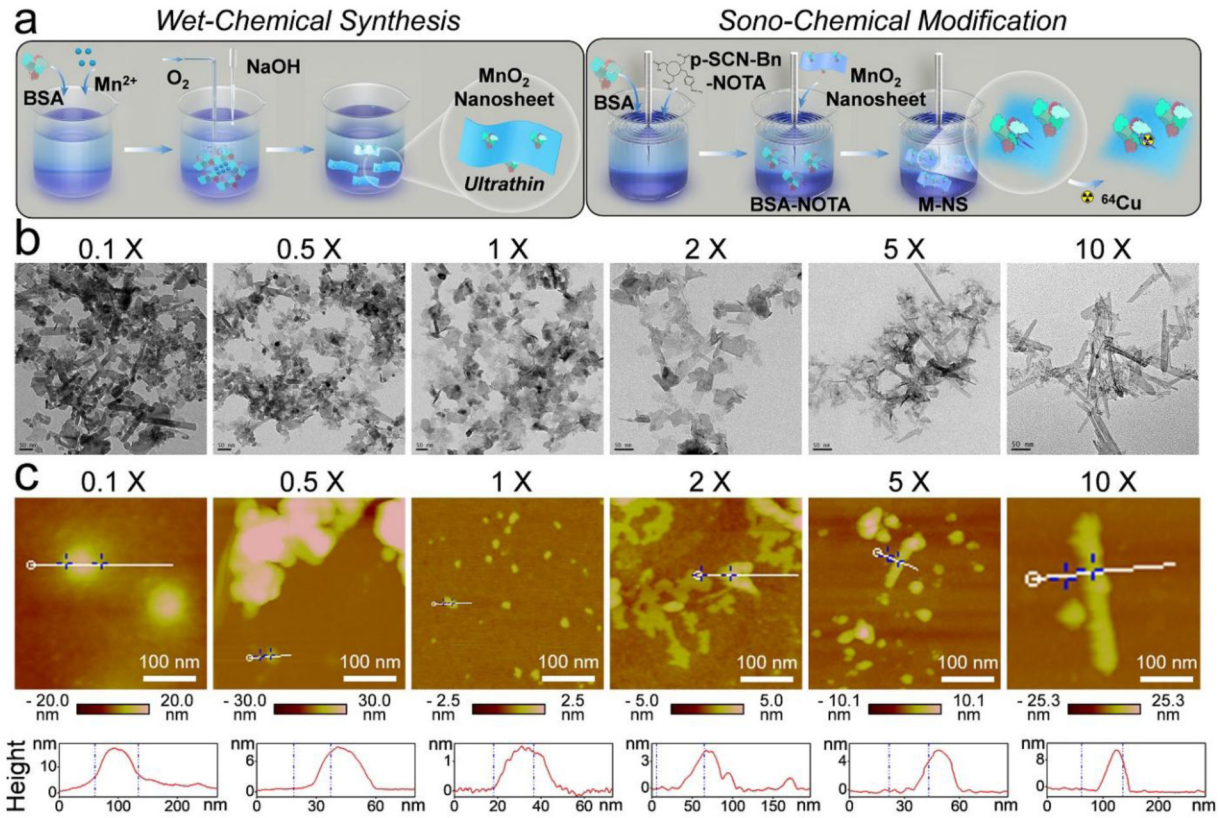

Figure 1.

Synthesis and morphology optimization of M-NS. (a) Schematic illustration of two-step synthesis of M-NS. First, a novel “wet-chemical method” was applied to form 2D nanosheets under the direction of BSA. Second, a unique “sono-chemical method” was introduced to further enhance the stability, biocompatibility, and surface functionality of the M-NS. (b) TEM images. Scale bar, 50 nm. (c) AFM images and height profiles of the M-NSs templated with an increasing dosage of BSA. The “0.1 X”, “0.5 X”, “1 X”, “2 X”, “5 X”, and “10 X” stands for a BSA dosage of 0.6, 3, 6, 12, 30, and 60 mg, respectively. Scale bar, 100 nm.

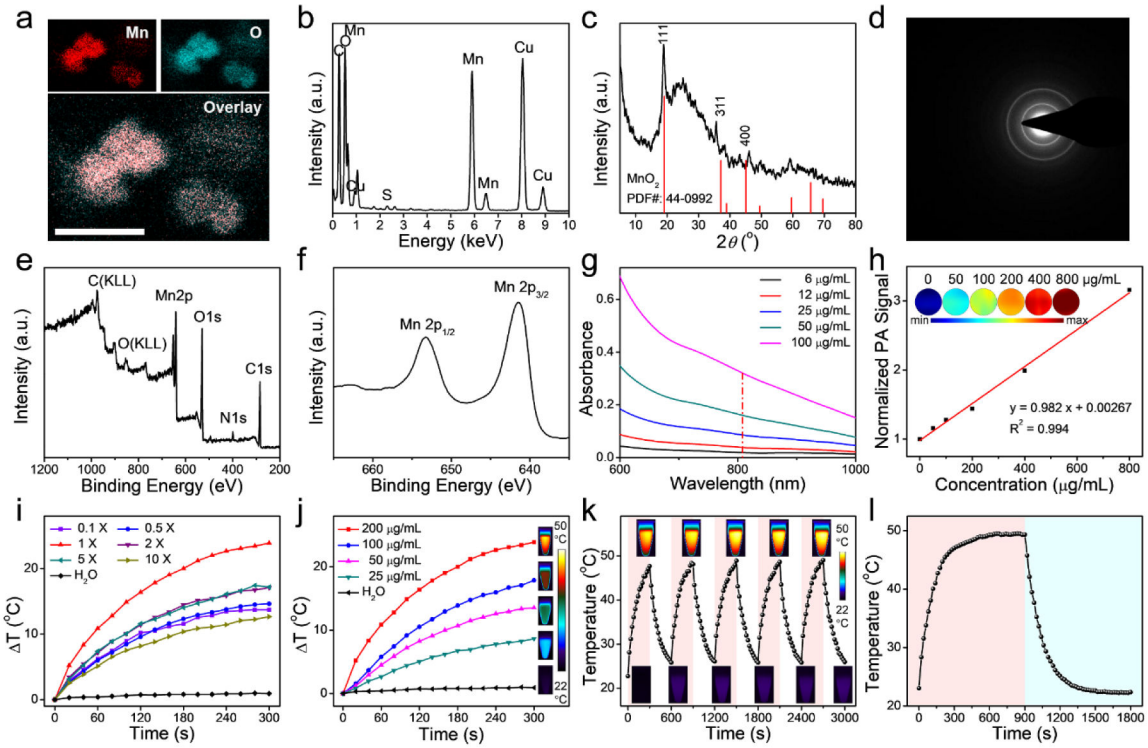

Figure 2.

Characterization of the optimized M-NS formulation (1 X). (a) Elemental Mapping. Scale bar, 50 nm. (b) EDS spectrum. (c) XRD analysis. (d) SAED pattern. (e) XPS data. (f) Mn 2p XPS spectrum. (g) UV-Vis-NIR absorbance spectra at various concentrations. (h) Plot of PA signals to concentration. Inset: PA images at elevated concentrations. (i) The optimization of MnO_2 morphology for photothermal effect. The 200 μg Mn/mL solutions of M-NS with different BSA dosages were irradiated (808 nm, 1 W/cm^2). (j) Concentration-dependent photothermal heating curves and images of the optimized M-NS (1 X). (k) Heating/cooling profiles for five repeated intervals of 5-min-on-5-min-off laser irradiations (808 nm, 1 W/cm^2). (l) Photothermal profile after laser exposure (808 nm, 1 W/cm^2) to reach a steady temperature and then to cool down by turning the laser off.

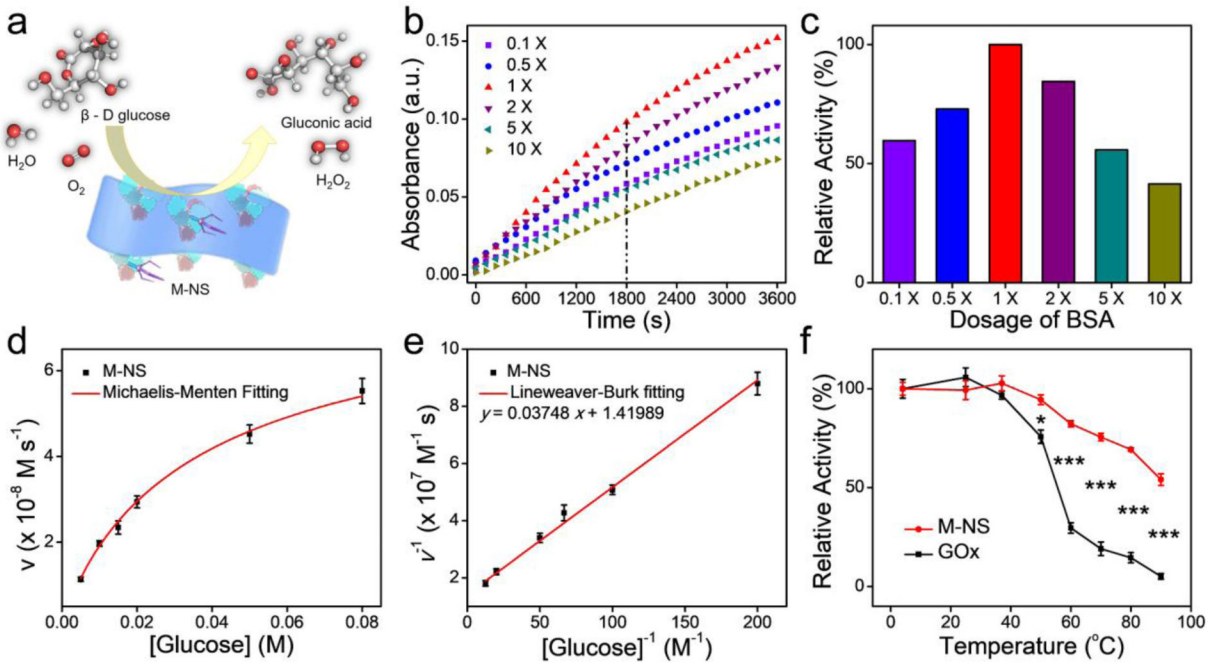

Figure 3.

GO*x*-like catalytic activity of M-NS (1 X). (a) Schematic illustration of the M-NS-catalyzed glucose depletion. (b) The optimization on MnO_2 morphology for the enzymatic activity. (c) Histogram of the relative activity within 30 min versus the dosage of BSA in the "wet-chemical synthesis". (d) Michaelis–Menten kinetics curve and (e) Lineweaver–Burk plotting of M-NS. (f) The thermal stability of nanozyme of the M-NS and natural enzyme of GO*x*. $*P < 0.05$ and $***P < 0.001$.

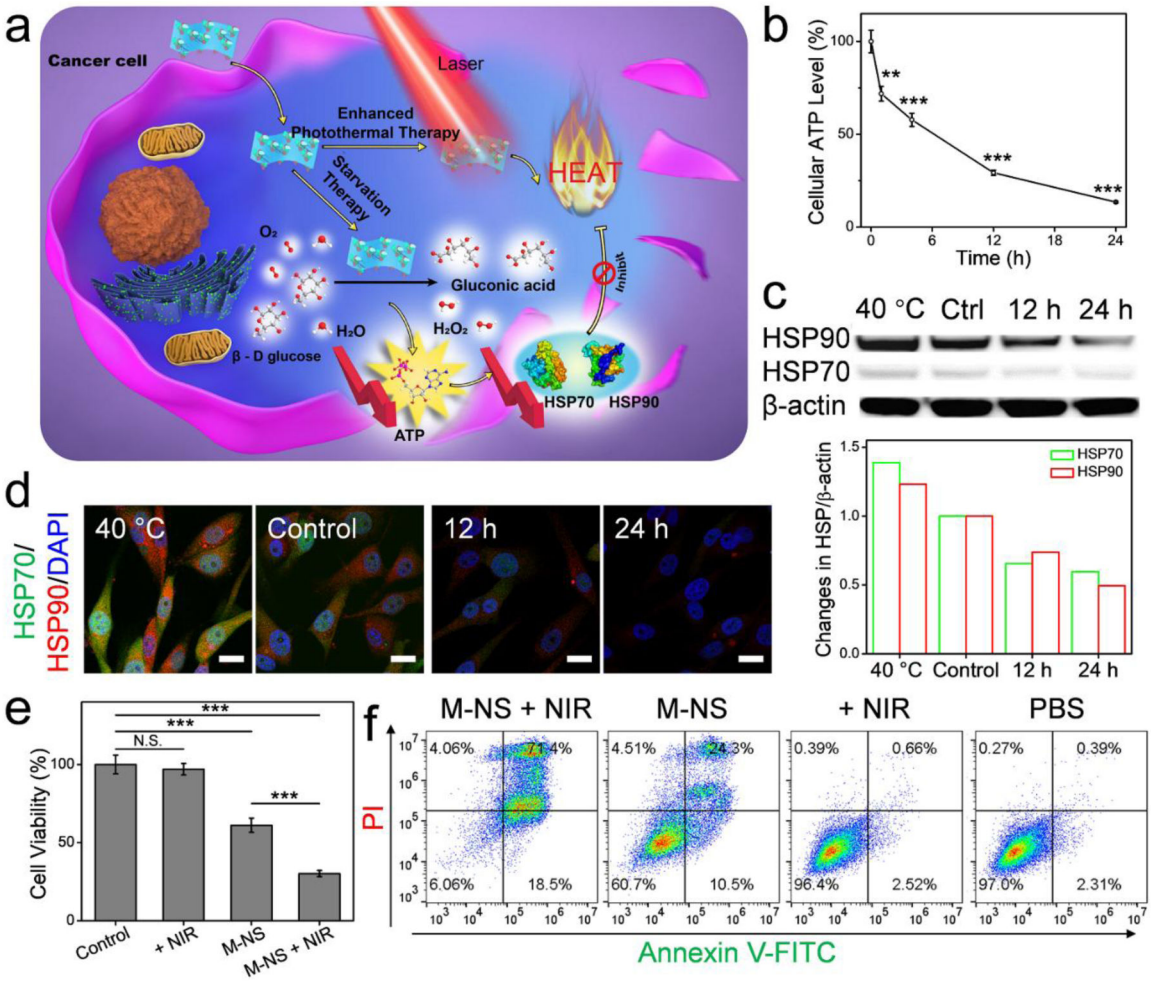

Figure 4.

In vitro studies. (a) Schematic illustration of the M-NS-mediated synergistically starvation-enhanced PTT in cancer cells. (b) Relative cellular ATP level of U87MG cells after incubation with the M-NS. (c) Western blotting analysis and (d) Confocal images of HSP70 and HSP90 expression in U87MG cells after treatment with M-NS for 12 or 24 hours. Cells incubated at 40 °C overnight were investigated as a positive control group. Scale bar, 20 μm. (e) MTT assays and (f) flow cytometry analysis on cells treated with M-NS plus an NIR irradiation. In controls, cells were treated with M-NS alone, irradiation alone, or PBS. *** $P < 0.001$.

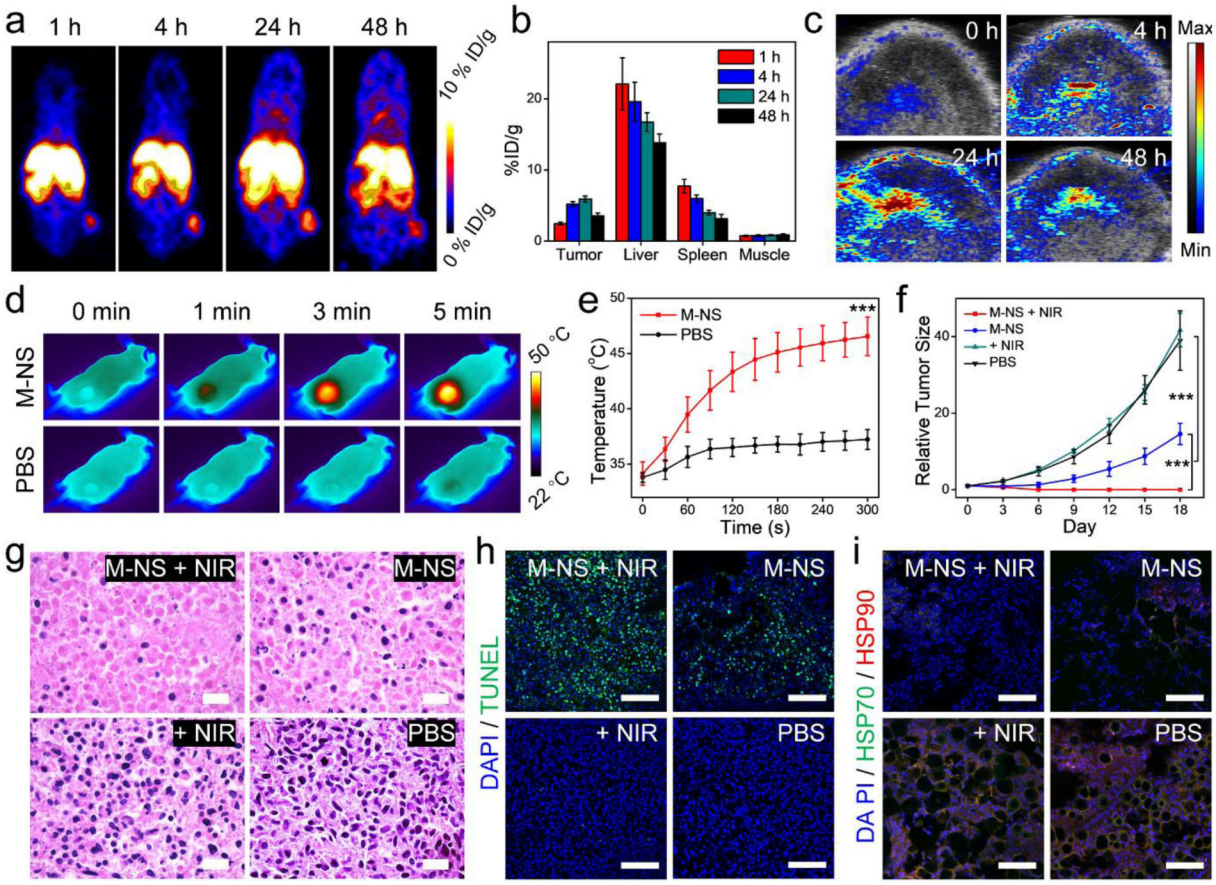

Figure 5.

In vivo studies. (a) Representative PET images after 1, 4, 24, and 48 h injection of ^{64}Cu-labeled M-NS into U87MG tumor-bearing mice. (b) PET quantifications on tumor, liver, spleen, muscle at selected time points based on (a). (c) Representative tumor PA images after the M-NS injection. (d) Thermographic images of mice upon a laser irradiation (808 nm, 1 W/cm^2) to tumors. (e) Temperature curves over the irradiation time at the tumor areas based on (d). (f - i) Therapy studies with M-NS on U87MG tumor model. (f) Tumor growth curves. (g) H&E staining, (h) TUNEL assays, and (i) Tumor HSP expressions after 24 h of the treatments. Scale bar, 100 μm. *** $P < 0.001$.